Electrochimica Acta 330 (2020) 135179

Contents lists available at ScienceDirect

Electrochimica Acta

journal homepage: www.elsevier.com/locate/electacta

Understanding the effect of *p*-, *n*-type dopants and vinyl carbonate electrolyte additive on electrochemical performance of Si thin film anodes for lithium-ion battery

Aliya Mukanova, PhD [a, **], Assel Serikkazyyeva [a], Arailym Nurpeissova, PhD [a], Sung-Soo Kim, PhD [b], Maksym Myronov, PhD [c], Zhumabay Bakenov, PhD [a, d, *]

[a] National Laboratory Astana, School of Engineering and Digital Sciences, Nazarbayev University, 53 Kabanbay Batyr Ave., 010000, Nur-Sultan, Kazakhstan
[b] Graduate School of Energy Science and Technology, Chungnam National University, 99 Daehak ave., Yuseong-gu, Daejeon, 34134, South Korea
[c] Physics Department, University of Warwick, Coventry, CV4 7AL, UK
[d] Institute of Batteries LLP, 53 Kabanbay Batyr Ave., 010000, Nur-Sultan, Kazakhstan

ARTICLE INFO

Article history:
Received 14 August 2019
Received in revised form
14 October 2019
Accepted 29 October 2019
Available online 31 October 2019

Keywords:
Silicon thin film
Anode
Dopant
Vinyl carbonate additive
Lithium-ion battery

ABSTRACT

Amorphous silicon (Si) is one of the most prospective high performance anode material for lithium-ion batteries and thin films of this material are promising for microbattery applications. Undoped, *p*- and *n*-type doped Si thin films were deposited by madgnetron sputtering on a three-dimensional current collector designed to accommodate the volume expansion of anode upon charge-discharge cycling, improve the active material adhesion, and to enhance the rate capability of the anode. The designed Si thin film anodes with and without doping were first investigated in lithium cell using various electrochemical techniques confirming the positive effect of doping on their performance. Raman spectroscopy was performed before and after cycling the electrodes to further elucidate such effects. The trends in change of an electrolyte during first lithiation/delithiation were observed by *in situ* Raman technique. Along with this, the morphology features of a solid electrolyte interphase (SEI) layer formed on the surface of the electrode and its modifications upon addition of 5% vinyl carbonate (VC) to the electrolyte were studied. The *n*-type doping and unique SEI layer formed with poly(VC) polymeric species suppressed the electrode crack formation preventing the capacity loss due to the material disintegration upon cycling, which resulted in an outstanding cycling performance of Si thin film with the capacity of 1305 mAh g^{-1} retained over 400 cycles.

1. Introduction

Silicon (Si) is the most promising anode material for next generation lithium-ion batteries (LIBs) due to its high theoretical specific capacity of 4200 mAh g^{-1}, which is 10 times higher than that of graphite (372 mAh g^{-1}). Si anode has a low working potential (~0.4 V *vs.* Li/Li^+); it is abundant, cheap and non-toxic [1–3].

Si anode undergoes large volume changes (more than 300%) during insertion and extraction of Li^+ ions which leads to the problems such as rapid material degradation, destruction of solid electrolyte interphase (SEI), and the electrical contact loss [4]. The cycling performance of Si anode improves with the decrease of its thickness, therefore Si in the shape of thin film is very attractive and promising as the anode for microbatteries [5]. The SEI formed at the electrode/electrolyte interface due to decomposition of the electrolyte breaks upon the material expansion [6] leading to a continuous electrolyte decomposition and performance degradation. The electrolyte composition affects the electrochemical properties of the electrochemical cell especially by influencing the SEI properties. Unsaturated compounds can be used as additives to nonaqueous electrolytes because they can easily undergo polymerization in the conditions of the electrochemical loads (reduction/oxidation). Such additives could enable controlling the formation of a stable SEI layer on the Si anode. The carbonate additives like fluoroethylene carbonate (FEC), vinylene carbonate (VC)

* Corresponding author.
** Corresponding author.
E-mail addresses: aliya.mukanova@nu.edu.kz (A. Mukanova), assel.serikkazyyeva@nu.edu.kz (A. Serikkazyyeva), arailym.nurpeissova@nu.edu.kz (A. Nurpeissova), kimss@cnu.ac.kr (S.-S. Kim), M.Myronov@warwick.ac.uk (M. Myronov), zbakenov@nu.edu.kz (Z. Bakenov).

https://doi.org/10.1016/j.electacta.2019.135179
0013-4686/

and propylene carbonate (PC) were proposed for improving the SEI layer morphology [7–10]. VC is one of the main promising representatives of unsaturated additives [11] which can be polymerized into poly(VC) on the electrode surface during charge/discharge process, strengthening the SEI layer and resulting in the cycling performance enhancement of the cell. In the same time incorporation of dopants into the silicon anode can noticeably affect its structural and electrical properties [12]. The roughened surface of the current collector has an ability to enhance the adhesion and prevent fast delamination and pulverization of the active material [13–15]. A combination of these approaches could result in a comprehensive solution of the Si anode problems towards development of a high performance Si thin film anode.

In this work we report on the design and study of the amorphous undoped, *p*- and *n*-type doped Si thin film anodes deposited on a three-dimensional (3D) substrate using magnetron sputtering. Raman spectroscopy helped to follow the structural features in Si thin film after dopants incorporation as well as after lithiation. The behavior of LPF_6-based electrolyte and *n*-type Si material during lithiation/delithiation was further observed by *in situ* Raman spectroscopy. The effect the VC electrolyte additive on the electrochemical performance and morphological changes of the SEI layer and Si film anode after galvanostatic cycling were carefully tested by atomic force microscopy (AFM) and scanning-electron microscopy (SEM).

2. Experimental part

2.1. Substrate preparation

The 3D surface was obtained on the rough side of a commercial Cu foil (9 μm, 99,99% MTI Co.) by etching in 5% ammonia solution for 23 h to produce a $Cu(OH)_2$ layer on the foil followed by the dehydration and Cu reduction as it was reported earlier [13]. The substrate preparation procedure is schematically shown in Fig. 1a.

Magnetron sputtering (LAB-18, Kurt J. Lesker Inc.) was chosen to deposit Si because this method allows obtaining the amorphous phase of Si (a-Si) easily. Three types of Si targets, undoped (>1 Ω cm), *p*-type doped (0.005–0.020 Ω cm) and *n*-type doped (<0.1 Ω cm) (99.999%, Kurt Lesker Inc.), were used for the films deposition. The conditions of sputtering were as follows: the base pressure ~1 10^{-8} Torr, power – 80 W(*rf*), working gas – Ar, work pressure – 5 mTorr, rotation – 5 rpm, deposition time – 60 min. The mass increment of Si was determined by weighing the samples before and after sputtering by an ultra-microbalance (MSE2.7S-000-DM, Sartorius) and constituted within 0.07–0.09 mg. Before assembling the cells, the materials were annealed in a mixture of Ar + H_2 (5%) gases at 300 °C in order to remove oxides and strengthen the adhesion between the Si film and the substrate [16].

2.2. Characterization

The obtained thin films were characterized by Raman spectroscopy (LabRAM HR Evolution, HORIBA) at the laser wavelength of 633 nm. The crystal structure of the samples were analysed using X-ray diffraction (SmartLab, Rigaku Co., Cu Kα radiation) over a 2θ range from 10 to 60°.

In situ Raman studies were performed using a modified flat cell (Hohsen Corp.) with an optically transparent glass window put on a drilled hole as shown in Fig. 1b. The samples of a liquid electrolyte and Si with electrolyte were sealed between two microscopic slides in order to obtain the separate spectra.

The electrical properties of a-Si thin films were studied by Hall effect measurement system (HMS5500/AHT55T5 Ecopia Co.). The thin films were deposited on a glass (1 cm^2) and the properties were registered at a current of 5 mA. The mean number of measurements was around 20 for each type of samples.

Scanning electron microscope (SEM, FeSEM Auriga Crossbeam 540, ZEISS) with a focused ion beam function (FIB) was used for morphological studies of the film samples surface and cross-section before and after cycling. The topological studies of SEI layers were performed by atomic force microscope (AFM, C3M SmartSPM™-1000, AIST-HT) in a tapping mode.

2.3. Cell assembling and electrochemical tests

Electrochemical experiments were performed using CR2032 coin cells (MTI Corp.) assembled in Ar-filled glovebox (LABmaster Pro, MBRAUN, <0.1 ppm H_2O and O_2). Lithium metal chips (99.9%, MTI Co.) served as both the counter and reference electrodes. A 1 M $LiPF_6$ solution in a mixture of ethylene carbonate, diethyl carbonate and ethyl methyl carbonate (1:1:1 v/v) was used as an electrolyte without VC additive. 5 vol% VC was added into the same electrolyte solution via 3 h stirring in Ar-filled glove box. Porous polypropylene (Celgard® 2400) was employed as a separator. For *in situ* Raman studies, the flat cell was assembled as shown in Fig. 1b. Galvanostatic charge/discharge cycling tests were carried out on an Arbin BT-2000 battery tester between 0.01 and 1 V at the current density of ~15 μA cm^{-2} at ambient temperature. All potentials given in the paper are referred to the Li/Li^+ electrode.

3. Results and discussion

In our previous work it was demonstrated that the porous current collector prepared by etching can noticeably delay Si film detachment and, therefore, prolong the cycle life of the anode [13].

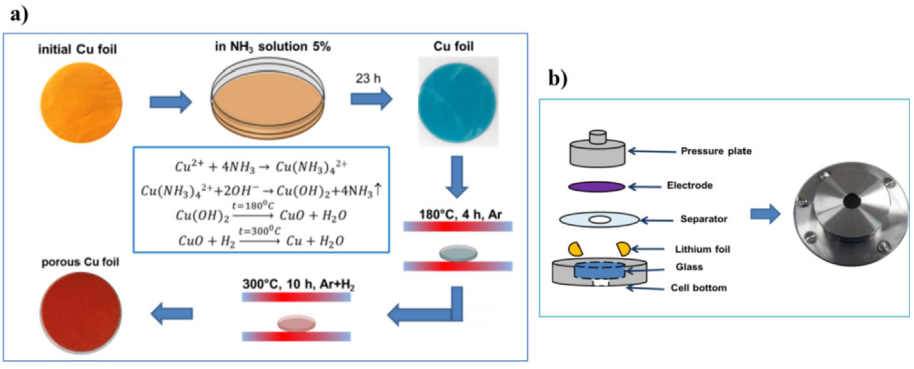

Fig. 1. Schematic illustration of (a) preparation of porous current collector; (b) cell parts and assembled modified flat type cell for optical *in situ* measurements.

Therefore, here we continued to use the same procedures coupled with the additional actions to improve a performance of Si thin film anode. SEM was used to follow the changes of the Cu surface during its treatment. As it can be observed from Fig. 2a the morphology of a commercial Cu foil was changed to a structure with the shrub-like outgrowth after etching (Fig. 2b). Consequently after dehydration, reduction, and cleaning of Cu (Fig. 2c) a well-formed 3D/porous structure was formed. Fig. 2d and e demonstrates the surface of Cu substrate with deposited Si, which constitutes of nanoscale spherical particles forming broccoli-like structure.

3.1. The doping effect on Si thin film anode cycling performance

In order to understand the doping effect on the cyclability and further improve the developed Si thin films, three types of Si films, undoped, and *p*- and *n*-type doped, were sputtered on the prepared substrate and studied as anodes in lithium half-cell using galvanostatic charge-discharge cycling. The structural and morphological characterization was made to identify the material properties as described further. Fig. 3 shows the results of the cycling tests at a current density of ~15 μA cm^{-2} in a voltage range of 0.01–1 V. Generally, from Fig. 3a, the potential profiles for the prepared thin film are typical for Si anode material. However, some differences in their cycling can be observed. The discharge and charge capacities of undoped Si anode gradually decrease up to 1402 mAh g^{-1} and 1356 mAh g^{-1} in the 50th cycle, respectively. The doped samples, *p*-type and *n*-type Si, exhibited similar discharge capacity of 1510 mAh g^{-1} and retained a slightly different charge capacities of 1482 mAh g^{-1} and 1486 mAh g^{-1} in the 50th cycle, respectively (Fig. 3a). In other words, although the initial capacities were almost the same for undoped and doped samples the capacity retention behavior was affected by doping. The influence of doping can be seen from the differential dQ/dV plots (Fig. 3b) demonstrating that the differential capacity of the undoped sample significantly reduced at the 250th cycle. It indicates that the reaction was of a low efficiency and a very low concentration of Li_xSi_y alloys phase was formed. For the *p*-type doped Si, the reaction still occurs at the 250th cycle while the *n*-type doped Si thin film demonstrated the highest ability for the phase transition. The 1st cycle in the differential capacity plots (dQ/dV) were equivalent for all Si samples.

Fig. 3c shows the cycling performance of the samples upon delithiation (charge capacity). It can be seen that the capacity retention is better for the *n*-type Si as a consequence of the observed cycling features described above. The *n*-type doped Si anode exhibited a stable capacity with no decay up to 170th cycle, with further gradual fading similarly to undoped and *p*-type samples.

The coulombic efficiency trends (CE, charge to discharge capacity ratio) for each sample can be seen in Fig. 3d. The CE is more stable for the *n*-type sample, which also found to be the highest up to the 200th cycle. The CE of *p*-type Si is similar to that of *n*-type with slightly lower values around 98.3%, whereas CE of the undoped sample had the lowest value of around 97.3%. During the rapid capacity fading between 130 and 200 cycles, all three types of material experienced significant fluctuations in CEs. Upon further cycling after the 200th cycle, when each cell experienced capacity fade, all the anodes exhibited an increasing in CE up to the final 400th cycle. The increase of CE is usually related to the completed formation of SEI layer, which prevents further parasitic reactions [19,20]. Therefore, it is suggested that an extensive material degradation and pulverization happened in the undoped Si led to the active material loss. Subsequently, in the considered cases, a sudden apparent increase of CE for the Si thin film anodes, indicating the enhanced reversibility of the Li^+ ions charge/discharge processes, can correspond to the material degradation followed by attenuation of the electrochemical reactions.

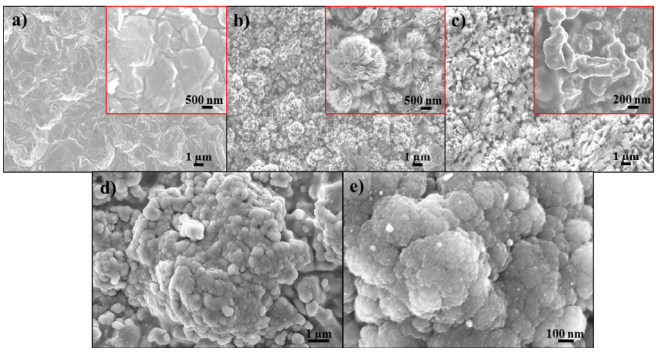

Fig. 2. SEM images of (a) rough Cu foil, (b) Cu after etching, (c) Cu after annealing, and (d,e) Si deposited on porous Cu.

Fig. 4 demonstrates the SEM images of *n*-type doped Si thin film anodes after cycling for 400 cycles. The doping type did not affect the morphological features of Si anodes after cycling. For all Si samples, the post-mortem SEM images looked similar (not shown here for undoped and *p*-type doped). From Fig. 4a, the extensive cracking can be observed on the anode surface. From the close view (Fig. 4b), it can be noticed that Si film contains the particles with the irregular morphology and significant porosity, i.e. the initial spherical shape of the particles (Fig. 2d) was changed dramatically. In order to investigate the cross-sectional morphology of Si thin film before and after cycling, FIB/SEM imaging was used. Comparing the images of as-deposited Si film (Fig. 4c) with that of the cycled Si anode (Fig. 4d), it can be clearly seen that the thickness of Si increased more than three times. The cross-section demonstrates the transverse cracks as well the film-substrate interface separation, i.e. Si detached from the Cu foil upon cycling.

In order to study the structural features of the Si anode after cycling, the Raman spectroscopy measurements were performed before (Fig. 5a and b) and after cycling (Fig. 5c and d). From Fig. 5a, the characteristic peaks of the pristine (not cycled) thin films are typical for the amorphous Si: the longitudinal optical (LO) mode of ~310 cm^{-1}, the longitudinal acoustic (LA) mode of ~400 cm^{-1}, the transverse optical (TO) mode at ~480 cm^{-1}, the overtone of the longitudinal and transverse phonons (2LA) at around ~630 cm^{-1} [21]. However, some differences were noticed for differently doped pristine Si thin films. The Gaussian fitting was applied (Fig. 5b) to investigate almost identical bands. One can see that the most scattering alterations in doped samples occurred at the LA, LO and 2LA bands. From the inset in Fig. 5b, it can be seen that there is a shift in the position of TO band of scattering for the *n*-type doped Si to the higher wavenumbers, while for the *p*-type Si, it has been shifted to the opposite direction. The LO and LA bands of the *n*-type Si also shifted to the right side according to the fitting results. This can be explained by the presence of phosphorus (*P*) impurity which causes the most intensive signal usually observed between 360 and 520 cm^{-1} [22]. For *p*-type doped Si film, 2LA peak had a wide left spreading with the position at 634 cm^{-1} which is presumably due to the influence of another impurity, boron (*B*), incorporated into the Si structure. The boron local vibrational peaks occur at a region of 550–680 cm^{-1} [23]. Similar features were earlier observed for the *B*- and *P*-doped crystalline Si nanowires [24].

Fig. 5c and d shows the spectra for the Si thin films in the lithiated state which were distracted from the cells after the third full lithiation (with a short exposure to the air). Fig. 5c demonstrates the alteration of the general spectra of Si thin films after cycling, where it can be noticed that the intensities of the curves in the regions of LA and LO bands of undoped and *p*-type Si have

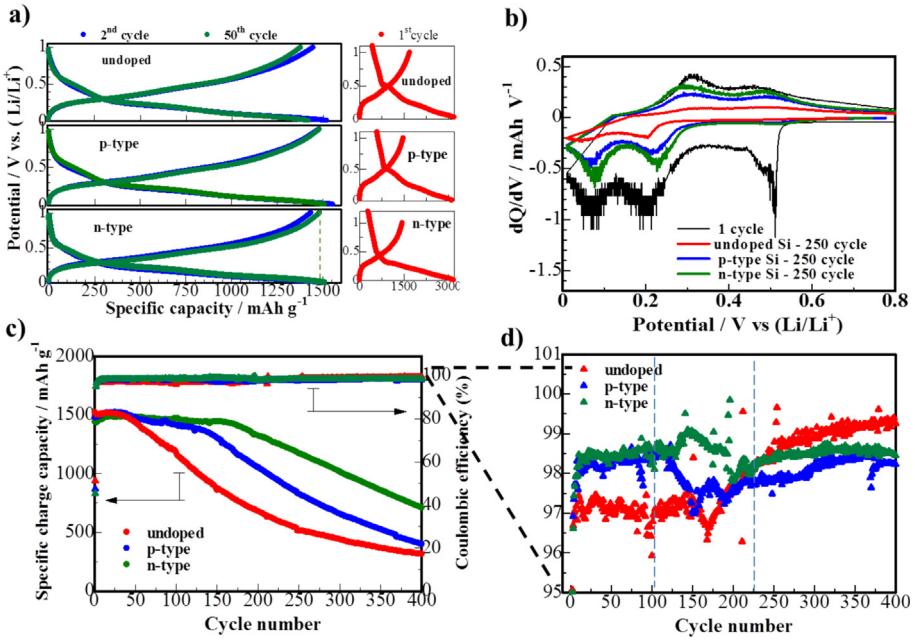

Fig. 3. Electrochemical performance of variously doped Si thin film anodes: (a) potential profiles, (b) differential capacity plots, (c) cycling performance, and (d) CE plot.

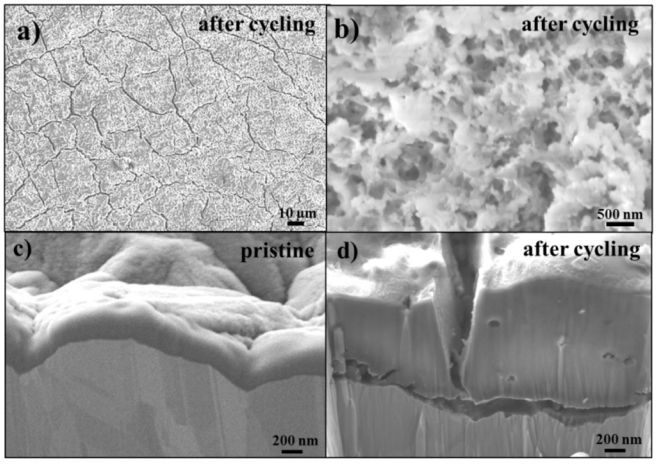

Fig. 4. Post-mortem analysis of *n*-type Si thin film (a,b) top view SEM after 400 cycles; FIB/SEM cross-sectional images of Si (c) pristine and (d) after 400 cycles.

increased significantly. From Fig. 5d, it can be noticed that fitted TO, LO and LA vibrations modes shifted, for all the samples, to the high wavenumbers and an intensity of the LO and LA peaks increased in contrast with the TO peak. More likely, this fact is due to the formation of Li_xSi_y in the material and Li_2O on the film surface, the signs of which are usually seen at higher shifts [25–27]. The 2LA peak position, in contrast, was moved in the back direction that also can be caused by the formation of lithium silicates around 610 cm^{-2} [25]. In order to prove the formation of Li_xSi_y alloys, the *ex situ* XRD measurements of lithiated samples has been performed. From Fig. 5e, it can be seen that the small peaks can be noticed on XRD spectrum at 20.5, 23.5, 29,38.5, 41.5 and 46 that are related to $Li_{15}Si_4$ alloy in an accord with literature data [28–31].

Table 1 summarizes the parameters, which were extracted from the fitting curves of variously doped Si film anodes before and after cycling. It can be seen that in the cycled samples the positions of peaks were changed significantly. The main TO peak increased for cycled samples; the highest climb was registered for the *p*-type sample. The shift of LO peaks happened for each type. However, it was higher for the *p*-type Si, while for the *n*-type sample it was the lowest increase. Considering LA peak, a big shift after cycling was observed for both undoped and *p*-type samples. The 2LA band decreased for the undoped and *p*-type, however, slightly increased for the *n*-type sample.

The second part of Table 1 represents the values of full width at half maximum (FWHM) for pristine and cycled samples. For the *n*-type Si film anodes, the FWHM of TO and LO scattering peaks have lower values, while the FWHM of LA is much higher. FWHM of 2LA for *p*-type is significantly wider than that of the two others. These were caused by the same reasons described for the positions of the peaks, i.e. the influence of the frequencies of B and P scattering photons which distorts the near-located LA, LO, and 2LA peaks. The general behavior of FWHM value for all bands of cycled samples was a decrease, except LA and 2LA bands, the FWHM values of which were found to decrease for all cycled Si samples.

The behavior of electrolyte and *n*-type Si electrode during lithiation/delithiation was observed by *in situ* Raman studies. Fig. 5f shows the Raman spectra of all components, Si, Cu, the electrolyte (1 M LPF_6 in EC:DEC:EMC), and binary system of Si with electrolyte. The main Si peak can be clearly seen at around 480 cm^{-1}; the scattering from the electrolyte is reflected by several peaks at around 741 cm^{-1} for $LiPF_4$, 940–980 cm^{-1} for EC and DEC components [32], 1110 cm^{-1} for Li_2CO_3 [33] and peak originated at ~570 cm^{-1}, which is more likely related to Li_2O [34]. The same peaks were observed in the spectra obtained from the *in situ* cell in Fig. 5g. Due to several components contribution to the spectra, the structural modification of Si could be hardly seen; however, the general behavior of Si-electrolyte system can be retrieved. From Fig. 5g, according to the trends of the Si peak at 480 cm^{-1} during lithiation/delithiation, there is an obvious decrease in the intensity upon the lithiation process. This can be explained by the beginning of alloying reaction and/or other irreversible reactions taking place at the first cycle.

Upon the lithiation process, the peak of Si becomes equal in height with the unchanged near-located peak at ~580 cm^{-1}. During

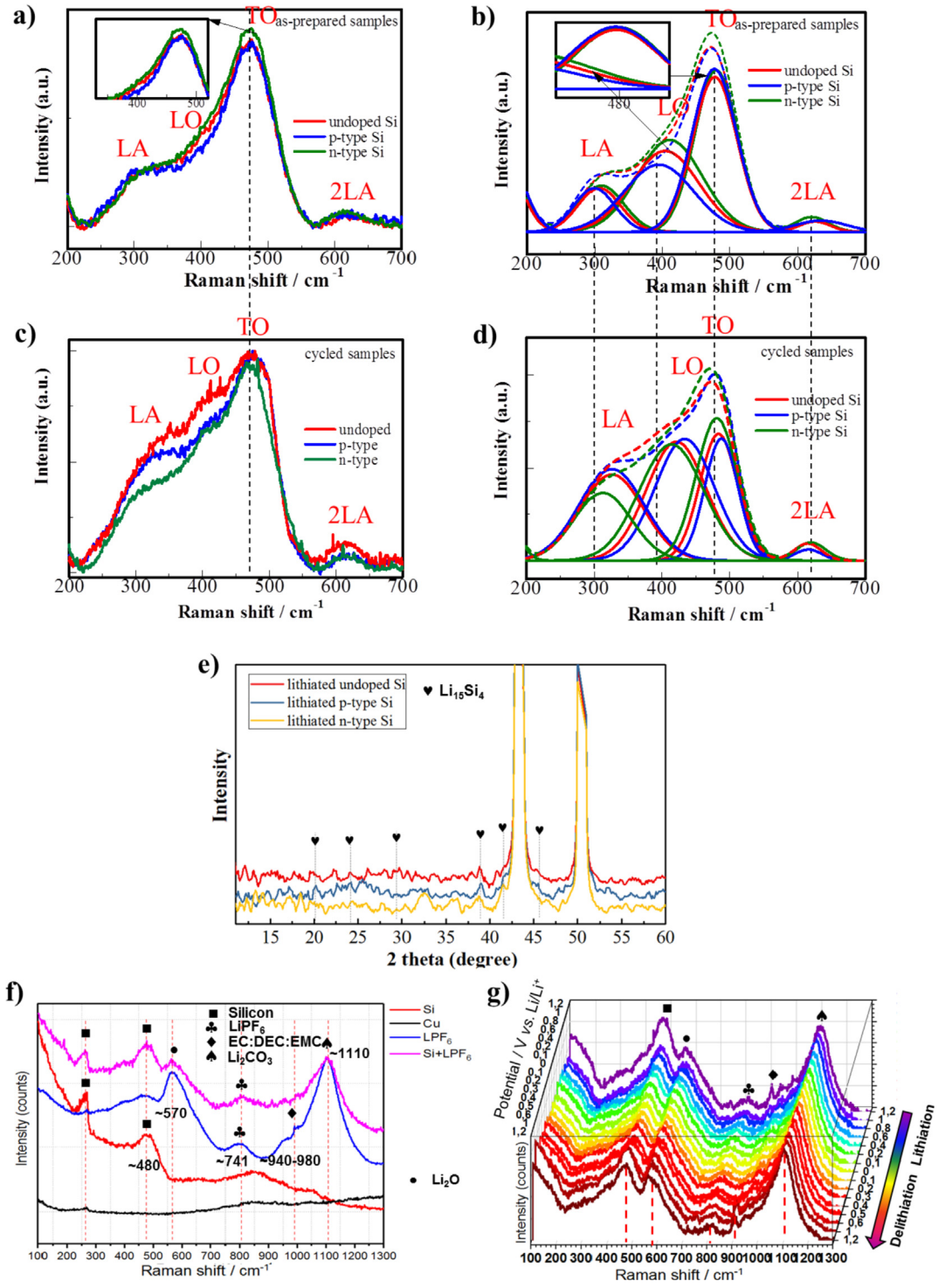

Fig. 5. Raman spectra of undoped, *p*-type and *n*-type Si thin films (a) before and (c) after cycling; and the fitting results (b) before and (d) after cycling. (e) XRD spectrum of the lithiated samples; (f) the separate spectra of the cell components, (g) *in situ* Raman spectra of the Si thin film anode during first cycle (CV at 0.3 mV s^{-1} in a potential range 0.01–1.2 V).

the delithiation, especially considering the last several spectra at 0.6–1.2 V, it can be noticed that the intensity of the Si peak is increasing again. The EC and DEC electrolyte components peaks positioned at around 980 cm^{-1}, disappear during the lithiation at the potentials below 1 V, and appear again at the same potential at the end of delithiation. This can be an indication of the reversibility of the EC and DEC participation in ongoing electrochemical processes, in particular, in the SEI formation.

Before electrochemical characterization, the investigation of electronic properties of Si thin film was performed. From the obtained results summarized in Table 2, it can be seen that the bulk and sheet carrier concentration is higher for doped samples, while the value for *p*-type Si is higher than that for *n*-type. It can be explained by the fact that the initial *p*-type target was doped up to

Table 1
The positions of the peaks on Raman spectra of variously doped pristine and lithiated Si thin film samples.

Peaks\Si type	undoped		*p*-type		*n*-type doped	
	pristine	cycled	pristine	cycled	pristine	cycled
peaks positions, cm^{-1}						
TO	477.8	480.3	477	487.9	479.7	481.2
LO	404	415.9	394.9	433.8	410.9	414.1
LA	306.8	332.3	299.4	325.6	309.8	312.5
2LA	625.2	618.7	634	615.7	620	619.6
full width at half maximum (FWHM)						
FWHM(TO)	76.7	66.6	78	57.9	74.5	72.8
FWHM(LO)	117	76.2	121	103.2	113	112.3
FWHM(LA)	73.2	111.7	70	113.1	77.7	99.6
FWHM(2LA)	54.3	54	89	46	58.4	51.6

higher levels (0.005–0.020 Ω cm) than *n*-type Si (<0.1 Ω cm). The results for resistivity, conductivity and mobility turned against the expectations. The resistivity was higher for the doped samples, while conductivity and mobility decreased. At low doping, the carrier concentration rises directly with doping concentration while the mobility reduces with doping hence the conductivity increases with the doping. At heavy doping levels, an increased fraction of the dopants does not experience ionization remaining inactive [35]. If the impurity content exceeds some limit, the dopants create the clusters in the material and the electron concentration does not increase further. These clusters do not behave as dopants (do not provide free electrons or holes) but as defects. This causes the additional scattering of electrons leading to a lower mobility [36–38]. The obtained values of the conductivity in the Si thin film can be compared with those existing in the literature [39].

In order to clarify the obtained results and to estimate the charge/discharge characteristics of doped Si negative electrodes, the electronic energy band diagram of the anode-electrolyte interface was considered (region between conduction (E_{CB}) and (E_{VB}) valence bands). At the first immersion of semiconductor into the electrolyte, the potential (Fermi level) is not equal between two different phases. In order to equilibrate this interface, the charge from one phase moves to another causing the "band bending" in the semiconductor phase [40]. Fig. 6 represents the energy levels at a semiconductor-electrolyte interface before and after contact for *n*-type and *p*-type doped semiconductors, respectively. After contact, the net result of equilibration is that Fermi level (E_F) in semiconductor becomes equal to that of electrolyte ($E_{F,redox}$) and a "built-in" voltage, V_{SC}, forms in Si.

For the *n*-type Si (Fig. 6a), the electronic charge consumed for Fermi level equilibration in the semiconductor comes from the donor impurities. The Si's Fermi level in the *n*-type Si decreases up to the same level as in electrolyte, while for the *p*-type Si, the Fermi level has to increase (Fig. 6b).

During the Li^+ insertion, an electron has to move to an unoccupied state in the host band structure. In *n*-type Si, the electron has to occupy a conduction band, whereas, for *p*-type Si, low energy valence band which is available [41]. This, in turn, can cause a delay of the charge flow in the *n*-type Si due to the higher potential barrier [42]. From the other hand, it was reported that the

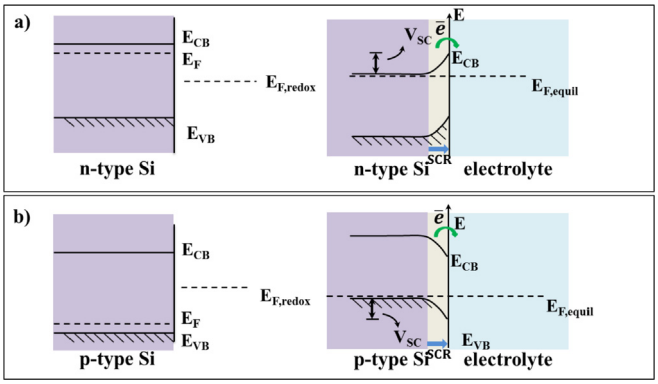

Fig. 6. The Si-electrolyte interface before and after equilibration (a) for *n*-type semiconductor and (b) for *p*-type semiconductor [40].

incorporation of B and P dopants may reduce the lattice spacing of crystalline Si that resulted in the rise of the Li^+ ions insertion energy [41,43]. It can be speculated that the dopants can affect the distance berween Si atoms in the amorphous state the same way. Taking into account the above considerations, Li^+ ions insertion into the *n*-type doped Si is energetically less preferably comparing with the *p*-type and undoped Si.

In our research, the Si thin films of the amorphous phase were prepared. Due to the high concentration of inactive impurities, the incorporation of dopants led to the decrease in conductivity and mobility in the *p*- and *n*-type Si films. As a subsequence, it was complicated to detect by structural investigation the decrease of Si–Si interatomic distances due to the incorporation of the dopants. However, considering the results of Raman spectroscopy of the variously doped lithiated Si, it was observed that *n*-type Si experienced less shift comparing to undoped and *p*-type Si. In fact, such suppression of the structural degradation can partially explain the longer cycle life of the *n*-type Si by the low energy increase of Li^+ ions insertion.

3.2. Effect of the electrolyte additive on the cycling performance of designed n-type Si anodes

The mechanism of VC interaction with the electrode materials was investigated previously [44–47]. The general process of VC anodic decomposition is proposed as follows: VC is reduced and a radical anion forms, which is followed by loss of CO_2 and formation of the vinyloxy radical anion, which initiates the polymerization of VC to generate poly(VC) via a radical polymerization reaction [48]. The residual vinyl group from the vinyloxy radical can polymerize via a mechanism of radical polymerization to produce the cross-linked polymer [46–48].

In this part we aimed to check to what extent VC can improve the performance of the prepared *n*-type Si thin film anode, which exhibited the best cycling performance in the first part of this work. Fig. 7 illustrates the results of the electrochemical tests of the *n*-type Si thin film anodes cycled with the VC-containing electrolyte (5 vol%). The VC-containing cell with *n*-type doped Si anode exhibited exactly the same capacity, cycling features and potential

Table 2
Electrical properties of variously doped Si thin film.

Si type	Bulk concentration (cm^{-3})	Sheet concentration (cm^{-2})	Resistivity (Ω cm)	Conductivity (Ω cm) $^{-1}$	Mobility ($cm^2V^{-1}s^{-1}$)
undoped	3.5×10^{18}	9.1×10^{13}	0.02	56.9	114.9
p-type	6.5×10^{18}	$2.8E\times10^{14}$	0.03	35.2	50.38
n-type	$4.9E\times10^{18}$	1.5×10^{14}	0.05	23.2	35.51

profile as it was shown for Si cycled without VC in Fig. 3a. From Fig. 7a, it can be observed that the differential capacity of Si thin film did not decrease during 250 cycles.

Fig. 7b shows the rate capability of the *n*-type Si thin film on porous Cu foil in the presence of VC in the electrolyte. Four initial cycles were obtained at the same current density of 15 μA cm^{-2} that was used in the above described electrochemical results. From the 5th cycle, the cycling current density was decreased up to 7 μA cm^{-2} which resulted in the capacity increase up to ~1901 μAh g^{-1}. Further the cell was cycled at a current density of 60 μA cm^{-2} delivering a capacity of 734 μAh g^{-1}, while at 120 μA cm^{-2} the cell capacity decreased to 245 μAh g^{-1}. However, when the current density of 15 μA cm^{-2} was applied again at the final stage of the experiment, the cell could regain the initial performance without significant capacity decay. The poor rate capability of the designed *n*-type Si anode can be resulted from the reduced electrical conductivity discussed in the first part of this section (Table 2).

Fig. 7c presents the cycling data for the cells with *n*-type Si thin film with/without VC additive (red/green). Obviously, the cycling performance of Si cycled with VC is significantly improved, retaining the capacity of 1305 mAh g^{-1} after 400 cycles against 709 mAh g^{-1} of the cell without VC. In fact, the obtained result is one of the top results in terms of capacity and number of stable cycles compared with other published data [49]. Fig. 7d shows the CE plot of two types of cells. One can see that CE for VC-containing cell is 99.3% in the first 100 cycles which further increases up to 99.7% upon the following cycles, which is higher than that of the cells without VC additive in the electrolyte. Besides, no data fluctuation was observed for the Si with the modified electrolyte reflecting prevention of the anode degradation and loss upon cycling.

EIS was used to investigate the effect of the VC additive on the electrochemical impedance of the Si film anode, and a consequent influence on its performance. Fig. 7e and f demonstrates the Nyquist plots for both, VC-free and VC-added electrolyte, respectively. The semicircle in the high-frequency region corresponds to a resistance of Li^+ ions diffusion through the formed SEI layer; the medium-frequency region part relates to a charge transfer resistance at the SEI and Si interface, while the low-frequency region is usually assigned to a Warburg diffusion impedance of Li^+ ions in Si and insertion capacitance accumulation of Li^+ ions into its bulk

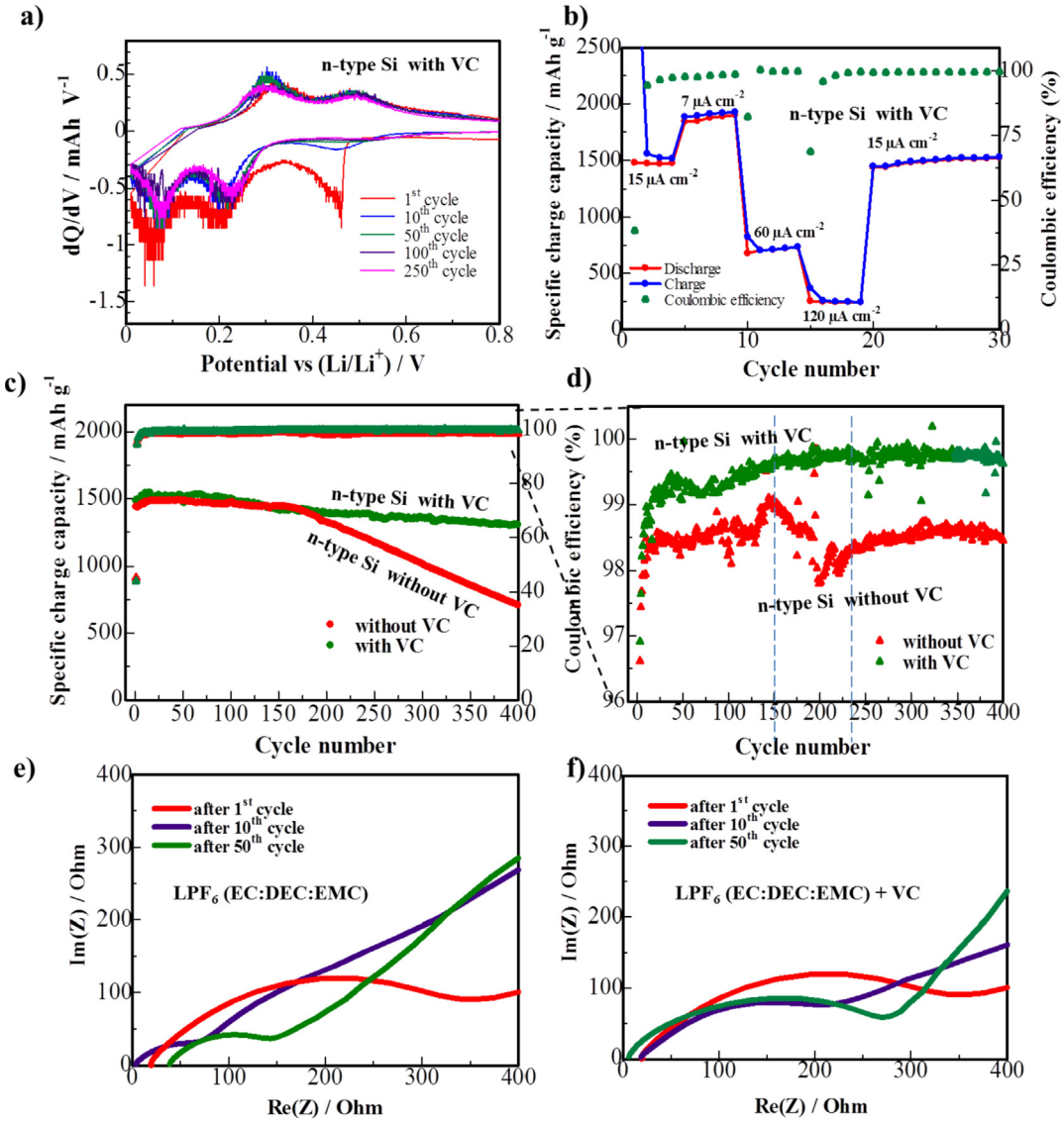

Fig. 7. Electrochemical test results for Si thin film anode in the presence of VC additive (a) differential capacity plot, (b) rate capability, (c) cycling performance, (d) CE plot; EIS of Si anode (e) without VC and (f) with VC.

[50]. From the graphs, it can be observed that the cells without and with VC demonstrate similar EIS trends upon cycling: EIS was almost identical for both cells after the first cycle, decreased after the 10th cycle and then again increased after the 50th cycle. However, for the cells with VC, the total impedance values over all cycles were higher than that of without VC. Chen et al. [50] reported on the stability of EIS for the initial 5 cycles for 1% VC-containing cells. In our work, we did not observe such stabilization and the impedance differed even from the 1st to 10th cycles. Our obtained data can be compared with another work where similar EIS trends were observed with 3% VC added into electrolyte [51]. It can be suggested that the increased concentrations of VC additive tend to slightly deteriorate the ionic conductivity of the Si anode that is more likely due to the higher amount of organic components in the composition of the SEI layer [47,52].

The morphology of the anode cycled in the presence and absence of VC additive was observed by SEM. Fig. 8a and b demonstrates the FIB/SEM images of the Si samples without/with VC additive after the 1st cycle. Si thin film cycled in the VC-free electrolyte (Fig. 8a) has the diverse morphology than another sample cycled in the VC-containing electrolyte (Fig. 8b). The top of the film expanded much more than the bottom part, besides the cracks can be seen in the bottom part of Si part adjacent to the substrate. From the cross-sectional image of Si film cycled with VC (Fig. 8b), one can see that Si is still uniform in thickness with some cracks between, and the SEI layer can be easily observed on the material surface. Fig. 8c–f shows the SEM images of the surface of post-mortem *n*-type doped Si thin film anodes which were cycled for 1 and 50 cycles without/with VC. It can be seen from Fig. 8c that after the initial cycle the SEI layer on Si cycled in VC-free electrolyte already has the cracks in contrast with a smooth SEI layer formed in the presence of VC (Fig. 8d). After 50 cycles, the cracks are more frequent in the VC-free SEI layer (Fig. 8e and g) than in the VC-containing system (Fig. 8f and h). In general, the SEI layer formed upon the decomposition of VC-containing electrolyte looked much stronger and more elastic. In fact, the VC additive favors the poly(VC) species generation during the electrolyte decomposition instead of lithium ethylene dicarbonate $(CH_2OCO_2Li)_2$, which is the major component in the SEI of common commercial electrolytes [53].

The topology of the SEI layer formed in both types of the cells was assessed using AFM. The surface of the VC-free SEI layer (Fig. 8i) looks rough after the 1st cycle and becomes smoother upon cycling, considering the images after 50 cycle (Fig. 8j). The roughness, in the beginning, could be originated from formation of the LiF crystals that are usually observed as separate particles in the SEI layer grown up with time [50,54]. After 50 cycles, the roughness disappeared that can be due to continuous growing of SEI layer which covers those crystal particles. The narrow prolonged cracks can be noticed on the sample. For the poly(VC)-containing SEI layer (Fig. 8k and l), the opposite trends of the topology changes were revealed: the SEI layer, being well formed and smooth in the beginning, acquired greater roughness with each subsequent cycle. More likely such different behavior can indicate the difference of the SEI layer formation mechanisms for these two types of samples. In the early reports [53], it was shown that VC exhibited a reductive current at a potential of ~1.25 V *vs.* Li/Li^+ that is much higher than for commercial electrolytes. It means that VC reacts first to form the

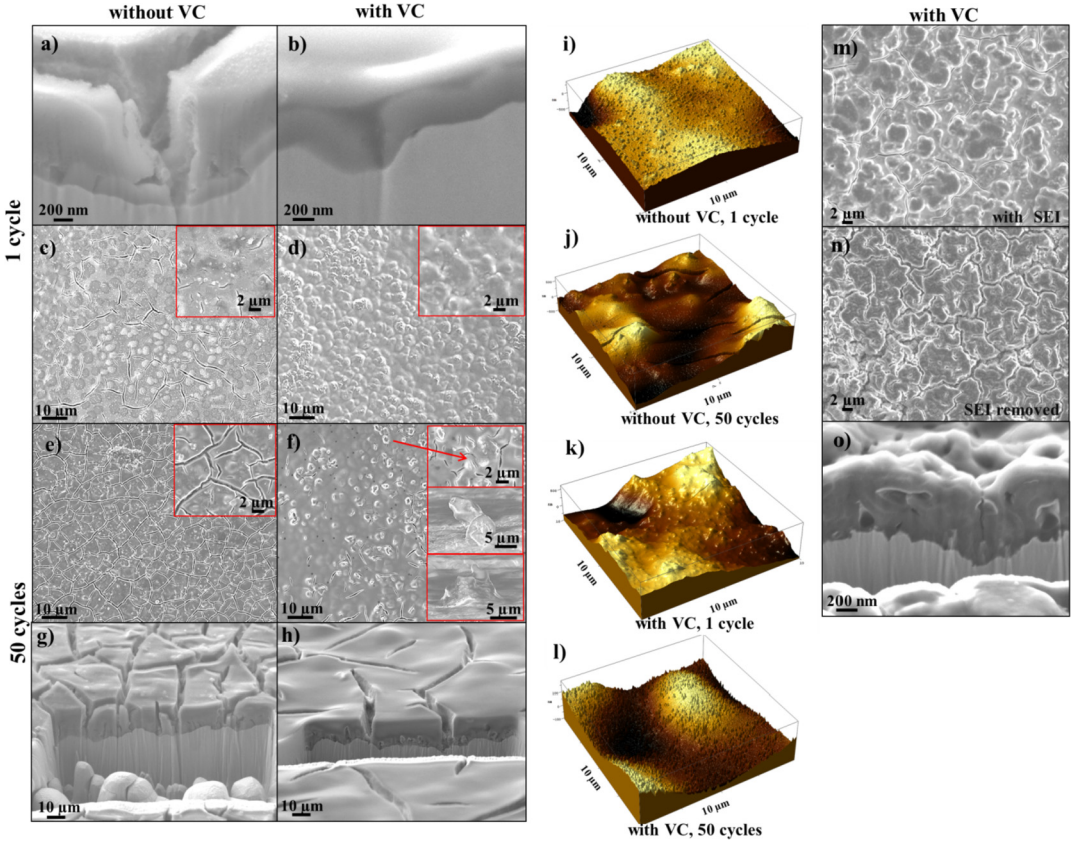

Fig. 8. Post-mortem studies. SEM analysis of SEI on Si thin film cycled in the cells after 1st and 50th cycles: (a,c,e,g) without and (b,d,f,h) with VC. AFM analysis of the surface of the Si thin film anodes cycled (i,j) without VC and (k,l) with VC for 1 and 50 cycles. (m,n) morphology of anode with and without SEI; (o) cross-section of the Si anode cycled with VC additive for 400 cycles.

SEI layer; therefore poly(VC) species will dominate in the SEI content as it has been revealed in another work [55]. Considering the insets on SEM image in Fig. 8f and AFM topology of VC-containing SEI in Fig. 8l, it seems that some particles are lying on the surface of SEI. Similar observations were reported previously for VC-containing SEI, where the particles were referred to LiF crystallites and/or oxides [56]. In fact, although it was reported that poly(VC) species inhibit the formation of LiF crystals, the latter anyway forms in the noticeable amounts that was revealed by XPS measurements [5,25,26]. Taking into account that VC-based SEI layer has already formed, it can be supposed that LiF crystals, usually formed at the lower potentials, can deposit on the SEI layer creating the surface roughness. However, from the closer view of the particles in Fig. 8f, it can be observed that the particles are not just lying on the surface but sometimes incorporated into SEI and even under it.

Fig. 8m–o illustrates the morphology and cross-section of the Si anode cycled with VC additive for 400 cycles. Comparing to the post-mortem images of the Si samples cycled in VC-free electrolyte (Fig. 4), one can notice a significant reduction of the material degradation. Fig. 8m shows the Si thin film cycled with the formed SEI, which is still in good condition with only a few cracks. When SEI was removed from the sample (Fig. 8n), the Si surface cracking can be observed. However, the distance between the cracks is not large and the morphology of the material was not critically damaged comparing with the data for the VC-free sample in Fig. 4a and b and no signs of material loss were observed. Fig. 8o shows the cross-section of the Si thin film which expanded noticeably but the delamination from the substrate was not observed. In general, from Fig. 8m–o, it can be seen that the surface of the sample became very rough with cycling. That is caused not only by the particles on the top of SEI (Fig. 8f) but also by the fact that the reorganization of the Si nanoparticles could happen under a strong SEI. We believe that the VC-containing SEI strongly restrained the Si during expansion and mitigated the materials pulverization upon cycling. Tightly holding Si thin film under it, a polymeric SEI layer does not allow releasing the stress during material expansion via extensive cracking/pulverization of the film. Instead, the build-up stress pushes the material to a rearrangement within itself. Thus, Si begins to fill the existing cracks, pores, and cavities in its own structure. These finding can be very important for the further development and preparation of stable Si-based anodes for the next generation Li-ion batteries.

4. Conclusion

In this work, the amorphous Si thin film anodes on the porous substrate were successfully designed and prepared. The study of the doping effect on the cycling performance clearly revealed that *n*-type Si works longer than undoped and *p*-doped samples. The *ex situ* Raman studies provided new data on the structural features of the pristine variously doped Si thin films as well as their structural changes in the lithiated state. *In situ* Raman studies demonstrated the reversibility of the EC and DEC components of the electrolyte upon discharge/charge processes.

The VC additive (5vol%) into LPF_6 based electrolyte was found to improve the Si thin film anode performance in terms of its mechanical stability and integrity according to the SEM studies results. It was suggested that the poly(VC)-containing SEI layer acted as a deterrent coating which helped to restrict the expansion of Si thin film as well as pushed the Si thin film to release the internal stress occurring during lithiation via morphological rearrangement in the film. This, in turn, prevented extensive pulverization and delamination of the active material. Thus, the designed *n*-type doped amorphous Si thin film could retain the capacity of 1305 mAh g^{-1} after 400 cycles.

Acknowledgements

The authors acknowledge the research grant AP05133519 “Development of 3-dimensional thin film silicon based anode materials for next-generation lithium-ion microbatteries” from the Ministry of Education and Science of the Republic of Kazakhstan and #SOE2019001 “Development of 3D all solid state thin film Li-ion microbatteries” from Nazarbayev University.

References

[1] K. Feng, M. Li, W. Liu, A.G. Kashkooli, X. Xiao, M. Cai, Z. Chen, Small 1702737 (2018) 1702737.
[2] X. Zuo, J. Zhu, P. Müller-Buschbaum, Y.-J. Cheng, Nano Energy 31 (2017) 113–143.
[3] Z. Zhou, L. Pan, Y. Liu, X. Zhu, X. Xie, Chin. Chem. Lett. 30 (2019) 610–617.
[4] Z. Zhou, Y. Liu, X. Xie, X. Ye, ChemComm 52 (2016) 8401–8404.
[5] H. Guo, H. Zhao, C. Yin, W. Qiu, Mater. Sci. Eng. B 131 (2006) 173–176.
[6] F. Ozanam, M. Rosso, Mater. Sci. Eng. B Solid-State Mater. Adv. Technol. 213 (2016) 2–11.
[7] A. Rezqita, M. Sauer, A. Foelske, H. Kronberger, A. Trifonova, Electrochim. Acta 247 (2017) 600–609.
[8] L. Liao, X. Cheng, Y. Ma, P. Zuo, W. Fang, G. Yin, Y. Gao, Electrochim. Acta 87 (2013) 466–472.
[9] T. Kennedy, M. Brandon, F. Laffir, K.M. Ryan, J. Power Sources 359 (2017) 601–610.
[10] S. Zhang, M. He, C.C. Su, Z. Zhang, Curr. Opin. Chem. Eng. 13 (2016) 24–35.
[11] J. Chai, Z. Liu, J. Ma, J. Wang, X. Liu, H. Liu, J. Zhang, G. Cui, L. Chen, Adv. Sci. 4 (2017) 16000377.
[12] S. Ohara, J. Suzuki, K. Sekine, T. Takamura, J. Power Sources 136 (2004) 303–306.
[13] A. Mukanova, A. Nurpeissova, S.S. Kim, M. Myronov, Z. Bakenov, ChemistryOpen 7 (2018) 92–96.
[14] A. Mukanova, A. Nurpeissova, A. Zharbossyn, S. Kim, Mater. Today Proc. 5 (2018) 22759–22763.
[15] A. Mukanova, A. Nurpeissova, A. Urazbayev, S. Kim, M. Myronov, Z. Bakenov, Electrochim. Acta 258 (2017) 800–806.
[16] L.B. Chen, J.Y. Xie, H.C. Yu, T.H. Wang, J. Appl. Electrochem. 39 (2009) 1157–1162.
[19] X. Yao, Q. Dong, Q. Cheng, D. Wang, Angew. Chem. Int. Ed. 55 (2016) 11344–11353.
[20] A. Wang, S. Kadam, H. Li, S. Shi, Y. Qi, Npj Comput. Mater. 4 (2018).
[21] V. Baranchugov, E. Markevich, E. Pollak, G. Salitra, D. Aurbach, Electrochem. Commun. 9 (2007) 796–800.
[22] Sijie Liu, N. Huo, S. Gan, Y. Li, Z. Wei, B. Huang, J. Liu, J. Li, H. Chen, J. Mater. Chem. C 3 (2015) 10974.
[23] N. Fukata, J. Chen, T. Sekiguchi, N. Okada, K. Murakami, T. Tsurui, S. Ito, Appl. Phys. Lett. 89 (2006) 203109.
[24] T.C. Yang, K. Nomoto, B. Puthen-veettil, Z. Lin, L. Wu, T. Zhang, Mater. Res. Express 4 (2017), 075004.
[25] L.S. Hoyos, B. Faroldi, L. Cornaglia, J. Alloy. Comp. 778 (2019) 699–711.
[26] T. Seuthe, M. Grehn, J. Bonse, M. Eberstein, H.J. Eichler, A. Mermillod-Blondin, Opt. Mater. Express 3 (2013) 755.
[27] A. Sifuentes, A.C. Stowe, N. Smyrl, J. Alloy. Comp. 580 (2013) S271–S273.
[28] T.D. Hatchard, J.R. Dahn, J. Electrochem. Soc. 151 (2004) A838–A842.
[29] I.A. Profatilova, T. Langer, J.P. Badillo, A. Schmitz, H. Orthner, H. Wiggers, S. Passerini, M. Winter, J. Electrochem. Soc. 159 (2012) A657–A663.
[30] Y. Wang, J. Dahn, J. Electrochem. Soc. 153 (2006) A2314.
[31] S. Iwamura, H. Nishihara, Y. Ono, H. Morito, H. Yamane, H. Nara, T. Osaka, T. Kyotani, Sci. Rep. 5 (2015) 25–27.
[32] S.M. Russell, O. Borodin, A.V. Cresce, J.A. Allen, J. Peng, K. Xu, M. Dai, M.P. Gobet, M.A. Schroeder, S.G. Greenbaum, R.E. Rogers, Phys. Chem. Chem. Phys. 19 (2016) 574–586.
[33] F.S. Gittleson, K.P.C. Yao, D.G. Kwabi, S.Y. Sayed, W.H. Ryu, Y. Shao-Horn, A.D. Taylor, ChemElectroChem 2 (2015) 1446–1457.
[34] R.S. Sánchez-Carrera, B. Kozinsky, Phys. Chem. Chem. Phys. 16 (2014) 24549–24558.
[35] R. Janssen, A. Janotta, Phys. Rev. B 60 (1999), 13561–1357.
[36] S. Paulo, Phys. Rev. B 43 (1991) 8946–8950.
[37] T.S. Ameshima, N.A. Ndoh, Y.A. Ndoh, Jpn. J. Appl. Phys. 44 (2005) 1186–1191.
[38] D. Caputo, G. De Cesare, Sol. Energy Mater. Sol. Cells 43 (1996) 263–272.
[39] P. Alpuim, V. Chu, R.A. Redol, J.P. Conde, J. Vac. Sci. Technol. A 19 (2001) 2328.
[40] K. Rajeshwar, in: A.J. Bard (Ed.), Encycl. Electrochem., Wiley-VCH Verlag GmbH & Co. KGaA, 2007.
[41] B.R. Long, M.K.Y. Chan, P. Greeley, A.A. Gewirth, J. Phys. Chem. C 115 (2011) 18916–18921.
[42] M. Lee, D. Yoon, U.J. Lee, N. Umirov, A. Mukanova, S. Kim, Front. Chem. 7 (2019) 389.
[43] Y. Domi, H. Usui, M. Shimizu, Y. Kakimoto, H. Sakaguchi, ACS Appl. Mater.

Interfaces 8 (2016) 7125–7132.
[44] L. El Ouatani, R. Dedryvère, C. Siret, P. Biensan, S. Reynaud, P. Iratcabal, D. Gonbeau, J. Electrochem. Soc. 156 (2009) A103.
[45] L. El Ouatani, R. Dedryvère, C. Siret, P. Biensan, D. Gonbeau, J. Electrochem. Soc. 156 (2009) A468.
[46] Y. Wang, S. Nakamura, K. Tasaki, P.B. Balbuena, J. Am. Chem. Soc. 124 (2002) 4408–4421.
[47] T. Jaumann, J. Balach, U. Langklotz, V. Sauchuk, M. Fritsch, A. Michaelis, V. Teltevskij, D. Mikhailova, S. Oswald, M. Klose, G. Stephani, R. Hauser, J. Eckert, L. Giebeler, Energy Storage Mater 6 (2017) 26–35.
[48] A.L. Michan, B.S. Parimalam, M. Leskes, R.N. Kerber, T. Yoon, C.P. Grey, B.L. Lucht, Chem. Mater. 28 (2016) 8149–8159.
[49] A. Mukanova, A. Jetybayeva, S.-T. Myung, S.-S. Kim, Z. Bakenov, Mater. Today Energy 9 (2018) 49–66.
[50] L. Chen, K. Wang, X. Xie, J. Xie, Electrochem. Solid State Lett. 9 (2006) A512–A515.
[51] C.C. Nguyen, B.L. Lucht, J. Electrochem. Soc. 161 (2014) A1933–A1938.
[52] S. Uchida, M. Yamagata, M. Ishikawa, J. Electrochem. Soc. 162 (2015) A406–A412.
[53] H.H. Lee, Y.Y. Wang, C.C. Wan, M.H. Yang, H.C. Wu, D.T. Shieh, J. Appl. Electrochem. 35 (2005) 615–623.
[54] A.M. Andersson, K. Edström, J. Electrochem. Soc. 148 (2002) A1100.
[55] L. El Ouatani, R. Dedryvère, C. Siret, P. Biensan, S. Reynaud, P. Iratçabal, D. Gonbeau, J. Electrochem. Soc. 156 (2008) A103.
[56] S.H. Lee, I.S. Jo, J. Kim, Surf. Interface Anal. 46 (2014) 570–576.